Multi-channel Electronic and Vibrational Dynamics in Polyatomic High-order Harmonic Generation

A. Ferré[1], A. E. Boguslavskiy[2,6], M. Dagan[3], V. Blanchet[1], B. Bruner[3], F. Burgy[1], A. Camper[4], D. Descamps[1], B. Fabre[1], N. Fedorov[1], J. Gaudin[1], G. Geoffroy[1], J. Mikosch[2,8], S. Patchkovskii[2,8], S. Petit[1], T. Ruchon[4], H. Soifer[3], D. Staedter[5], I. Wilkinson[2], A. Stolow[2,6,7], N. Dudovich[3], and Y. Mairesse[1]

[1] *Université de Bordeaux - CNRS - CEA, CELIA, UMR5107, F33405 Talence, France*
[2] *National Research Council Canada, 100 Sussex Dr, Ottawa, ON K1A 0R6, Canada*
[3] *Department of Physics of Complex Systems, Weizmann Institute of Science, Rehovot 76100, Israel*
[4] *CEA, IRAMIS, Lasers, Interactions and Dynamics Laboratory - LIDyL, CEA-SACLAY , F-91191 Gif-sur-Yvette, France*
[5] *Université de Toulouse - CNRS, LCAR-IRSAMC, Toulouse, France*
[6] *Department of Physics, University of Ottawa. 150 Louis Pasteur ON K1N 6N5, Canada*
[7] *Department of Chemistry, University of Ottawa. 10 Marie Curie ON K1N 6N5, Canada and*
[8] *Max-Born-Institute, Max-Born-Strasse 2A, 12489 Berlin, Germany*
(Dated: March 2, 2022)

High-order harmonic generation in polyatomic molecules generally involves multiple channels, each associated with a different orbital. Their unambiguous assignment remains a major challenge for high-harmonic spectroscopy. Here we present a multi-modal approach, using unaligned SF_6 molecules as an example, where we combine methods from extreme-ultraviolet spectroscopy, above-threshold ionization and attosecond metrology. Channel-resolved above-threshold ionization measurements reveal that strong-field ionization opens four channels. Two of them, identified by monitoring the ellipticity dependence of the high-harmonic emission, are found to dominate the harmonic signal. A switch from the HOMO-3 to the HOMO-1 channel at 26 eV is confirmed by a phase jump in the harmonic emission, and by the differing dynamical responses to molecular vibrations. This study demonstrates a *modus operandi* for extending high-harmonic spectroscopy to polyatomic molecules, where complex attosecond dynamics are expected.

In the simplest view of molecular strong-field ionization, the most probable valence electron to be removed by a strong laser field is the most weakly bound one, namely that from the highest occupied molecular orbital (HOMO). This assumption is based on quasi-static, single active electron pictures and the exponential decay of the tunnel ionization probability through a field-suppressed Coulomb barrier [1]. However, even in a quasi-static picture, the tunnel ionization probability also depends on the spatial structure of the molecular orbital [2, 3]. Furthermore, more than one electron could get driven coherently by the laser field. The time scales of electron motions in molecules may not be fast compared to the laser period and the adiabatic approximation inherent to the quasi-static picture may fail: non-adiabatic multi-electron (NME) dynamics can ensue [4]. Consequently, strong field ionization of molecules is significantly more complex than from atoms, with possible contributions from multiple channels, leaving the ion in a coherent superposition of electronic states. Such ionic excitation can result in multi-electron processes and ultrafast charge migrations on an attosecond timescale [5, 6].

The signatures of multi-channel ionization in above threshold ionization (ATI) [7] and high harmonic generation (HHG) [8–10] are fundamentally different. In ATI, different channels produce different electron energy combs. The relative energy shifts of these combs depend on both the ponderomotive energy, reflecting the laser intensity, and the vertical ionization potential of the channel in question. The contributions of different channels, each leading to an energy-shifted ATI comb,

are incoherently summed in the detected photoelectron signal. In contrast, in HHG, the different ionization channels connect the same initial and final states (*i.e.* neutral ground electronic state) and therefore their contributions are coherently summed in the harmonic emission (Fig. 1). The HHG mechanism can thus be described as a multi-channel interferometer. The weights of the interfering paths are determined by the ionization yields and the recombination dipole moments [11, 12]. Resonances in the recombination process (e.g. due to the presence of an auto-ionizing state or a shape resonance) strongly increase these dipole moments in specific energy ranges. The relative phases of the interfering paths are complex and have important contributions from all steps of the process. Hence, the HHG mechanism can serve as an extremely sensitive probe which coherently encodes the contribution of the different quantum paths involved in the process – providing rich spectroscopic signatures of the strong field light matter interaction.

Since the contribution of small amplitude channels is enhanced by the interferometric nature of the process, high-harmonic spectroscopy has the potential to resolve strong field multi-electron phenomena with extremely high sensitivity. However, this task imposes significant challenges. To date, the identification of channels in HHG has been demonstrated in small linear (diatomic or triatomic) molecules via the manipulation of the molecular alignment angle with respect to the generating laser polarization [5, 6, 13–15]. For polyatomic molecules, field-free 3D alignment is achieveable [16] but remains challenging in general. Therefore we propose a
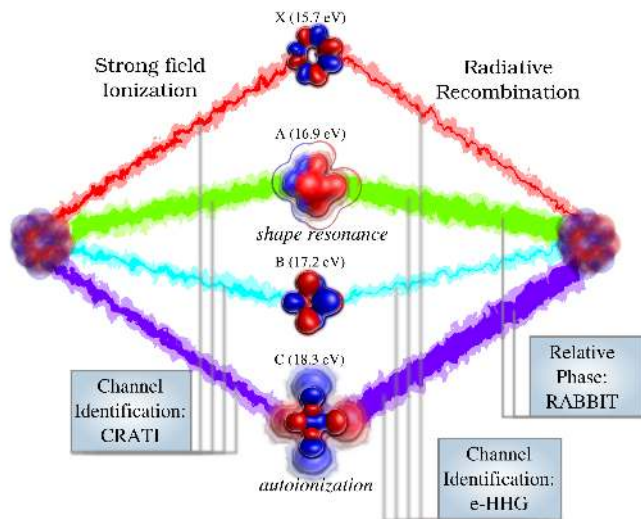
FIG. 1: Schematic view of multi-channel HHG. Multiple open channels in strong-field ionization are identified with the Channel-Resolved ATI (CRATI) technique. The ionization potential of each channel is indicated next to the schematic view of the associated molecular orbitals. The radiative recombination process is modified by the presence of resonances, increasing some of the channels' contribution to the harmonic emission. These dominant channels are identified by elliptically-driven HHG (e-HHG). The relative phase between the dominant channels is measured by RABBIT.

more direct control over the multi-channel interferometer, illustrated in Fig. 1. Can we control the relative contributions from each arm? Can we identify the phases associated with the different paths? In the following, we directly address these issues.

In this letter, we combine complementary strong field measurements to develop a *multi-modal* high-harmonic spectroscopy. To illustrate this, we chose a polyatomic system in which many channels can contribute to the harmonic emission: SF_6, whose four highest occupied molecular orbitals (each multiply degenerate) lie within less than 3 eV. Due to its symmetry (O_h point group), this system cannot be aligned in the laboratory frame. The identification of the channels contributing to HHG and the measurement of multi-channel ionization dynamics is thus particularly challenging.

In order to discern the ionization mechanism, we performed channel-resolved ATI (CRATI) measurements on SF_6 [17] for laser wavelengths ranging from 800 to 400 nm, revealing that at least four channels contribute to the strong-field ionization (Fig. 1). Using high-harmonic spectroscopy, we introduce a new experimental method for identifying channels based on HHG with elliptically polarized light. The analysis of this reveals a clear transition between two dominant channels around 26 eV. Furthermore, we used RABBIT measurements (Resolution of Attosecond Beating By Interference of Two-photon transitions [18]) to reveal the possible influence of res-

onances in the HHG process [19]. Finally we induced vibrational dynamics in the ground electronic state of SF_6 (via stimulated Raman pumping) in order to explore the influence of molecular geometry on the different channels. The results of these experiments, corroborated by state-of-the-art ab-initio calculations,

allowed us to identify the HOMO-1 and HOMO-3 ionization channels as the major contributors to HHG in SF_6.

I. RESULTS

A. Strong-field ionization channels in SF_6

ATI and HHG are closely related sub-cycle ionization phenomena. In ATI, strong field ionization (SFI) releases electrons into the continuum around every maximum of the laser electric field. This is repeated every optical cycle throughout the pulse. As a result, the photo-electron spectrum shows discrete peaks separated by the driving laser frequency ω. The position of the peaks of this ATI comb is set by both the ionization potential and intensity dependent terms (channel-dependent Stark shifts, ponderomotive shifts U_p): $KE_{e^-}^j = n\hbar\omega - I_p^{j(s)} - U_p$, where $I_p^{j(s)}$ is the Stark shifted (s) ionization potential of ionization channel j, and n is an integer. At constant intensity, the ATI combs of different channels give a direct measurement of their relative ionization potentials. In polyatomic molecules, where electronically excited cation states tend to undergo field-free fragmentation, different ionization channels can yield different fragments. This means that measuring the ATI spectrum associated with a given fragment, using covariance or coincidence detection, provides direct identification of the SFI channel or channels.

The CRATI technique, however, measures the channel I_p modulo the photon energy. In general, if the energy difference between two ionization channels matches the photon energy of the driving laser, the ATI combs will be overlapping. More specificallyn, if the frequency of the driving laser field is resonant with a single- or multi-photon transition in the neutral or the ion, the ATI combs will also be overlapping. Therefore, in order to resolve the SFI channels, we varied the laser wavelengths between 400 and 800 nm (see Methods). This enabled us to follow the position of the ATI combs as a function of wavelength. The results are shown in Fig. 2, where the ATI spectra associated with the dominant SF_5^+ fragment are shown for each laser wavelength. The diagonal lines indicate the expected position of the ATI peaks associated with the four lowest electronic states of the ion, for absorption of 7 to 11 photons. Clearly, multiple channels are present at all wavelengths. However, for the 800 nm driving field, the multi-channel nature of the strong-field ionization process is obscured by the cation electronic states having energy level spacings which happen to be multiples of the driving field frequency. Therefore, for the case of SF_6, the variation of the driving field fre-
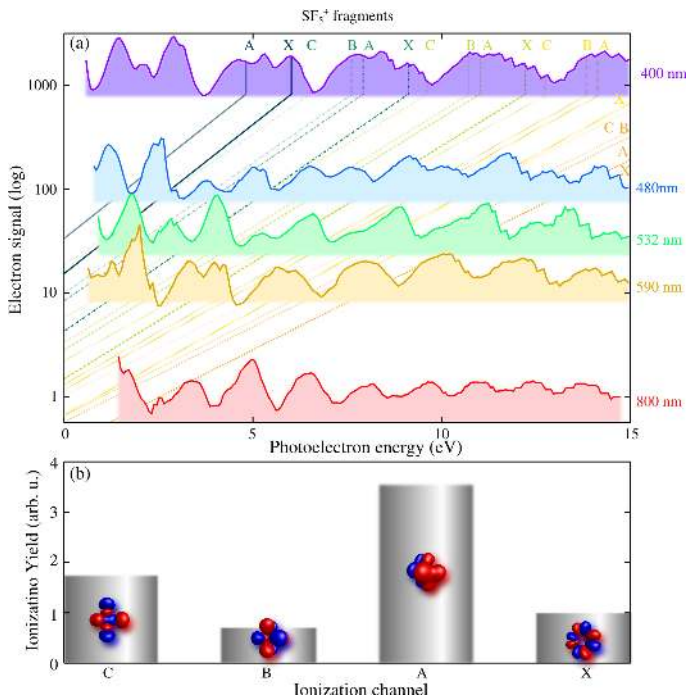
FIG. 2: (a) Channel-Resolved Above Threshold Ionization (CRATI) spectra of SF_6 at different laser wavelengths. Note that the spectra correspond to the SF_5^+ fragment; the ground state of SF_6^+ is unstable. The spectra are shifted vertically proportional to the laser photon energy. The diagonal lines indicate the expected position of ATI peaks from different ionization channels, for absorption of 7 (dark blue), 8 (blue), 9 (green), 10 (yellow) and 11 (orange) photons. (b) Calculated ionization yield for different channels at 800 nm. The X, A, B and C states are the ground and first three electronically (doublet) excited states of the cation.

quency was required in order to resolve the multiple SFI channels involved.

The CRATI measurements show that four main channels are involved in strong field ionization of SF_6, at all wavelengths. Quantifying the relative weight of these different channels would require knowledge of the branching ratios to each associated fragment. Unfortunately, these are unknown. In order to theoretically determine these weights, we calculated the tunnel ionization probability P_{ion}^j for each channel j by using a previously described approach [20, 21] and averaging over all molecular orientations. Ionization calculations used a 1/2-cycle 800-nm $\sin^2$ pulse at 10^{14} W/cm^2 peak intensity. The resulting weightings are shown in Fig. 2 (b). Two main factors determine the channel SFI rates: (i) the ionization potential of the channel – the ionization rate decreases exponentially with I_p; (ii) the topography of the ionizing molecular orbital – nodes in the plane perpendicular to the laser polarization tend to suppress the ionization probability. The first effect was long considered to be dominant: SFI mainly occurs from the highest occupied molecular orbital, even though deeper channels can

be observed under specific conditions, such as in aligned molecules. However, in a CRATI study of n-butane [17], it was shown that excited state channels dominate over the ground state channel, despite their higher I_ps. The results from Fig. 2(b) are alike due to geometrical effects in SFI of SF_6 which overcome the exponential dependence on I_p, even for unaligned targets.

B. Calculation of channel-resolved high-harmonic generation

SFI involving multiple channels generates multiple interfering pathways in high-order harmonic generation. The harmonic signal is determined by the coherent sum over all possible channels (see Fig. 1). In the following, we present a simple model of HHG in which the SFI channels are considered to be uncoupled. Specifically, we assume that there are no sub-cycle non-adiabatic multi-electron transitions (NME) which would coherently couple cation states: an electron leaving a given cation electronic state will recombine to the same state.

The harmonic dipole moment is determined by the SFI probability, the propagation of the electron in the continuum, and the recombination cross section [11, 12]. The propagation in the continuum induces a dephasing of the harmonic emission, corresponding to the phase accumulated by the molecule between ionization and recombination. This is given by $\varphi^j = \Delta I_p^j \tau$ [22, 23], where ΔI_p^j is the difference between the ionization potential of the channel under consideration and the ground state ionization channel (X), and τ is the electron propagation time in the continuum, which increases with harmonic order from 0.6 fs to 1.7 fs for short trajectories at 800 nm. We make the approximation that the recombination dipole moment d_{rec}^j is equal to the field free XUV photoionization dipole moment. This was studied experimentally using synchrotron radiation and was the subject of accurate theoretical modelling [24]. The simulated photoionization cross sections from [24] are shown in Fig. 3(a).

The harmonic intensity $I^j = \left| P_{ion}^j d_{rec}^j e^{i\varphi^j} \right|^2$, calculated for each channel, is shown in Fig. 3(b). The picture, which is very complex in the case of photoionization where many channels have similar cross sections (Fig. 3(a)), appears to be simplified by SFI. The tunneling probability from the highest occupied molecular orbitals is significantly reduced by the presence of nodes in the orbitals, such that deeper channels are favoured, as illustrated in Fig. 2(b). As a result, the harmonic signal is dominated by two channels, C and A, respectively below and above 25 eV. This property is quite remarkable: due to its sensitivity to tunnel ionization, high harmonic spectroscopy can isolate channels which may be difficult to distinguish in photoionization experiments (for instance, the A and B channels are not distinguished in XUV ionization). The maxima of the dominant channels are related to resonances in the photoionization cross section:
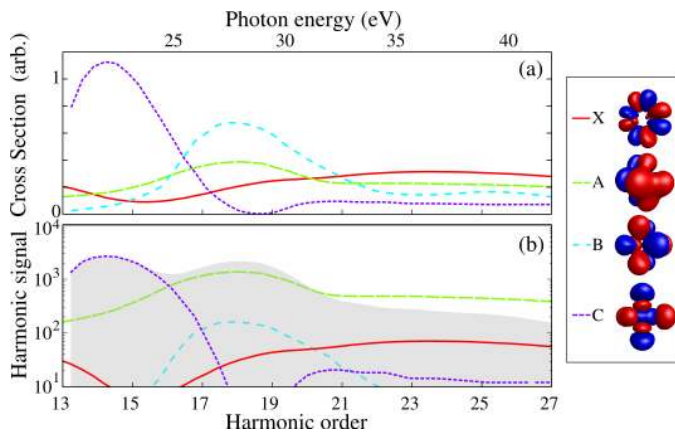
FIG. 3: (a) XUV photoionization cross sections from [24]. (b) Calculated harmonic intensity from different channels, and net response obtained by coherent superposition of all channels (gray area). The inset at right shows the highest occupied molecular orbitals corresponding to the different ionization channels.
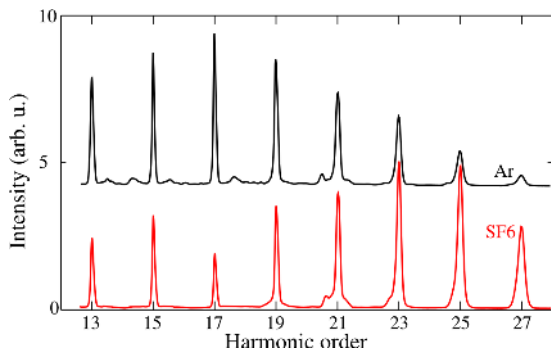

FIG. 4: Harmonic spectra generated in Ar (black) and SF_6 (red) at $I \approx 1.3 \times 10^{14}$ W/cm^2. The argon spectrum is vertically shifted in order to improve visibility.

an autoionization resonance for channel C ($5a_{1g} \rightarrow 6t_{1u}$) and a shape resonance ($1t_{2u} \rightarrow \epsilon t_{2g}$) for channel A [25, 26].

The total harmonic intensity is calculated by coherently summing the signals from the different channels (Fig. 3(b)). The result shows a minimum between H15 and H17 of the 800 nm, around 25 eV. Changing the laser intensity modifies the electron propagation times in the continuum and therefore the relative phase φ^j between channels. As a result, the shape and contrast of the minimum are modified, but its position is hardly affected.

C.   Experimental determination of SFI channels

Signatures of multi-channel contributions are readily observed in the HHG spectrum. In Figure 4, we show an experimental harmonic spectrum generated in SF_6 using 800 nm pulses at $I \approx 1.3 \times 10^{14}$ W/cm^2. In order
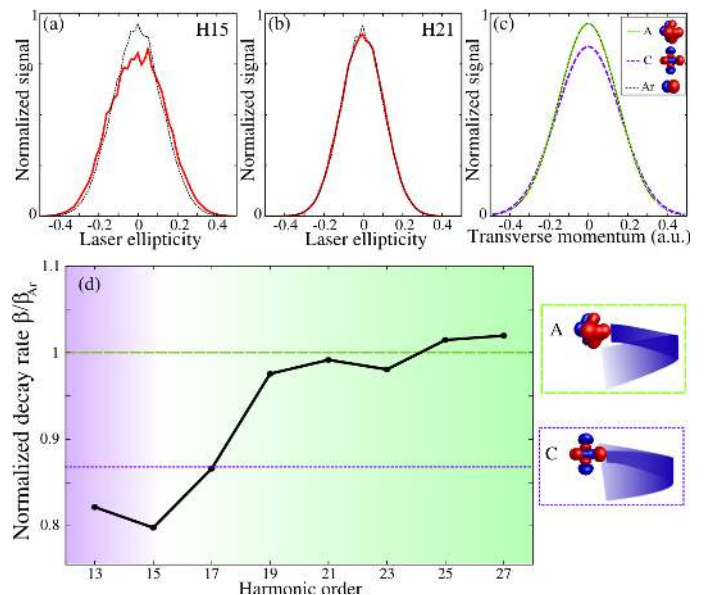

FIG. 5: The identification of SFI channels using elliptically polarized HHG. Measured harmonic signals as a function of laser ellipticity for H15 (a) and H21 (b) in argon (black dashed) and SF_6 (red continuous). The curves are normalized to the same area. (c) Calculated electron transverse momentum distribution in argon and the A and C channel from SF_6. (d) Measured response of the harmonic signal as a function of laser ellipticity in SF_6, normalized to that in Ar. The horizontal dashed lines are the theoretical normalized ellipticity-dependent responses for the A (green) and C (purple) channels, respectively.

to distinguish the simple, single-orbital picture from the multi-channel case, we compared our measurement with argon, an atomic system with a similar ionization potential to the HOMO of SF_6. The SF_6 spectrum extends to higher orders and shows a pronounced minimum at harmonic 17, as was previously observed at a lower laser intensity [27]. Varying the laser intensity in our experiment does not modify the position of this minimum, as expected from our simple model. This minimum is a first indication that points towards a transition between channels C and A at around 25 eV (Fig. 3 (b)). However, a definite identification of such a transition requires new methods in high-harmonic spectroscopy. These are discussed below.

How can we identify the involved channels without needing a full theoretical model of the harmonic emission? Such identification requires a differential measurement, a measurement which reveals the response of the molecular system to a variation of the laser parameters. This can be achieved by measuring the variation of the harmonic signal with laser ellipticity, ϵ. The measured harmonic signal as a function of laser ellipticity in argon and in SF_6 is shown in Fig. 5(a-b). The harmonic intensity decays exponentially with ϵ^2 [28] and can be fitted by a Gaussian $I_q(\epsilon) = I_q^0 e^{-\beta_q \epsilon^2}$, where q is the

harmonic order and β_q the variation with ellipticity. The ellipticity-dependent responses of argon and SF_6 are remarkably similar for harmonic 21 whereas that of argon is higher for harmonic 15.

High-order harmonic emission in an elliptical laser field can be described in a quasi-static semi-classical picture, as follows. First, electrons tunnel out of the molecule with a finite transverse momentum distribution. This distribution is dictated by the molecular orbital structure, filtered through the tunneling process [29]. If the electron wavepacket at the exit of the tunnel is spatially localized, then the momentum distribution is broad. The transverse momentum distributions associated with argon and the A and C channels in SF_6, calculated using the approach described in [29], are shown in Fig. 5(c). The distributions have a Gaussian profile, with the same width for argon and the A channel, while the C channel shows a broader distribution. This is consistent with the more localized character of the HOMO-3 (C) rather than the diffuse HOMO-1 (A). During propagation in the continuum, the electron wavepacket spreads transversly. The spread of the returning electron wavepacket depends on the time spent in the continuum (and thus on the harmonic order, the lowest harmonics being emitted before the highest harmonics [30]), but also on the initial transverse momentum distribution: the broader the initial transverse momentum distribution, the broader the returning wavepacket. With an elliptically polarized driving field, the orthogonal component of the field shifts the electron in the lateral direction, leading to a suppression of the recollision probability. Such suppression depends on both the trajectory length and the initial channel-specific transverse momentum. Therefore, the harmonic response β as a function of ellipticity serves as a fingerprint of the molecular orbital, i.e. of the SFI channel.

The variation of β_{SF_6}/β_{Ar} with harmonic order is shown in Fig. 5(d). Normalization to the response of argon suppresses the linear dependence of the ellipticity response with harmonic order, which simply reflects the change in electron trajectory length. Above H17, the ellipticity responses of SF_6 and argon are remarkably similar, while they differ by $\sim 20\%$ for H15 and below. Theoretical ellipticity responses are calculated using Gaussian fits of the distributions shown in Fig. 5(c) and reported, in Fig. 5(d), upon normalization to the argon response. They are in good agreement with experiment, given the simplicity of the model, and confirms the transition between the A and C channels at H17.

D. Measurement of the relative phase between channels

Elliptically-driven HHG in SF_6 revealed a transition in the channel dominating the emission process: harmonics 15 and below are produced by the C channel whereas harmonics 17 and above are produced by the A channel. In the following we use attosecond metrology to determine
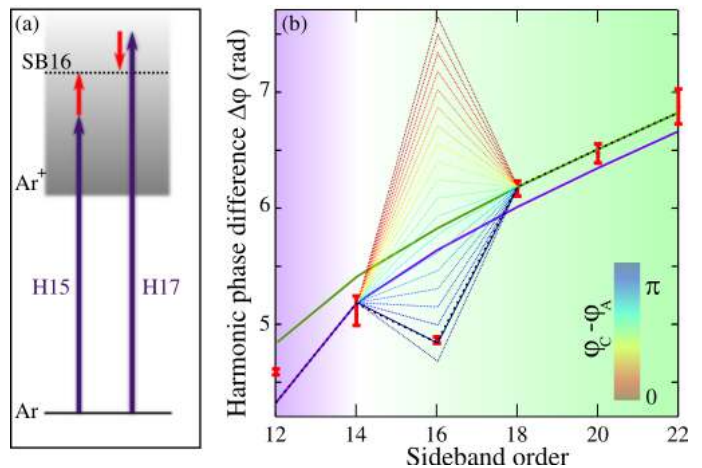

FIG. 6: Measurement of the relative phase between HHG channels. (a) Principle of the RABBIT method: high harmonics photoionize argon atoms in the presence of an infrared (800 nm) field. Absorption of harmonic 15 and one IR photon, or absorption of harmonic 17 and stimulated emission of one IR photon both lead to the production of the same sideband (SB16) in the photoelectron spectrum. (b) Phase of the sideband oscillations as a function of the delay between IR and harmonics. The experimental data points (with error bars) and theoretical results (solid lines) from saddle point analysis for the A (green) and C (purple) channels. To account for the response at SB16, we consider a transition from A to C channels between harmonic 15 and 17 (black dots). In this case, the relative phase between the two channels determines the magnitude of the signal for SB16. The dotted lines are the results of simulations as a function of relative phases $\varphi_C - \varphi_A$ varying from 0 to π by steps of 0.05π. It can be seen that the experimental data agrees with the simulations for a relative phase of 0.95π.

the relative phase between these two channels.

The RABBIT technique [18] is an attosecond pulse characterization method which measures the relative phase between consecutive harmonics. RABBIT is based on photoionization of a target gas by high-order harmonics, in the presence of a weak fundamental laser field. The photoelectron spectrum shows main lines, resulting from the absorption of harmonics, and sidebands, corresponding to absorption of one harmonic and absorption or emission of an infrared photon (Fig. 6(a)). Two quantum paths involving two consecutive harmonics lead to the same sideband, which results in an interference process. The sideband intensity thus oscillates as a function of delay between harmonics and the IR. The phase of this oscillation Φ_q^{SB} encodes the relative phase between the neighbouring harmonics $q + 1$ and $q - 1$: $\Phi_q^{SB} = \Delta\varphi_q + \Delta\phi_q^{at}$, where $\Delta\varphi_q = \varphi_{q+1} - \varphi_{q-1}$ is the phase difference between harmonics $q + 1$ and $q - 1$ and $\Delta\phi_q^{at}$ is a scattering phase intrinsic to the target (the atomic phase, i.e. the phase accumulated by the photoionized electron in the atomic scattering potential [18]).

In Figure 6(b), we show the measured harmonic phase

difference obtained using SF_6 as a generating gas and argon as a detecting gas. The harmonic phase difference increases with harmonic order but a clear deviation is observed at SB16, reflecting a specific phase difference between harmonic 15 and 17. A similar behavior was reported in [31]. Calculations of the harmonic phase, within the Strong-Field Approximation and using the Saddle Point method, were performed for the two channels expected to dominate the harmonic emission in this energy range: the A (green) and C (purple) channels. The resulting harmonic phase difference shows a similar increase with harmonic order for the two channels, reflecting the temporal dispersion of electron trajectories leading to emission of different harmonics [30]. The calculations are in good agreement with the experiment for SB 18 to 22, associated with channel A, and for SB 12-14, associated with channel C. We note that a transition from the C to A HHG channels between harmonic 15 and 17 would produce a shift in the phase of sideband 16. The electron trajectory leading to a given harmonic order slightly differs between the two channels, and this difference is enough to induce a significant effect on the phase accumulated along the whole trajectory. However, the results from this model do not agree with the experimental data: the calculated $\Delta\varphi$ for SB16 is around 1.3 rad while the measured phase shift is 4.8 rad. This shows that there is an additional dephasing of the harmonic emission between channels A and C which is directly measured by experiment. Therefore, the simulations were repeated with the introduction of an additional variable phase shift $\varphi_C - \varphi_A$ as an adjustable fit parameter (Fig. 6 (b)). Excellent agreement with the experiment is obtained when $\varphi_C - \varphi_A = 0.95\pi$. Importantly, this phase difference arises from the phases of the recombination matrix elements in the HHG process. Its determination illustrates the strength of this interferometric method in revealing the effects of shape resonances, autoionizing states and ionization phases in HHG [19].

E. Response of different channels to molecular vibrations

We have identified the different channels operating in HHG from SF_6 by manipulating the electron trajectories in the generating mechanism. In the following, we vary the nuclear degrees of freedom via vibrational excitation, resulting in systematic modification of all stages of the 'interferometer'. As discussed below, this further highlights the multi-channel nature of the HHG process.

Small molecular structural changes in the generating medium can induce significant modifications in the high-harmonic emission. For instance, Raman pump - strong-field probe experiments in SF_6 showed that the intensity of harmonic 25 to 45 varies by $\sim 10\%$ upon molecular vibration [32], even if the bond length variations remain small ($\sim 1\%$). Molecular vibrations may significantly change both the amplitude as well as the phase of each
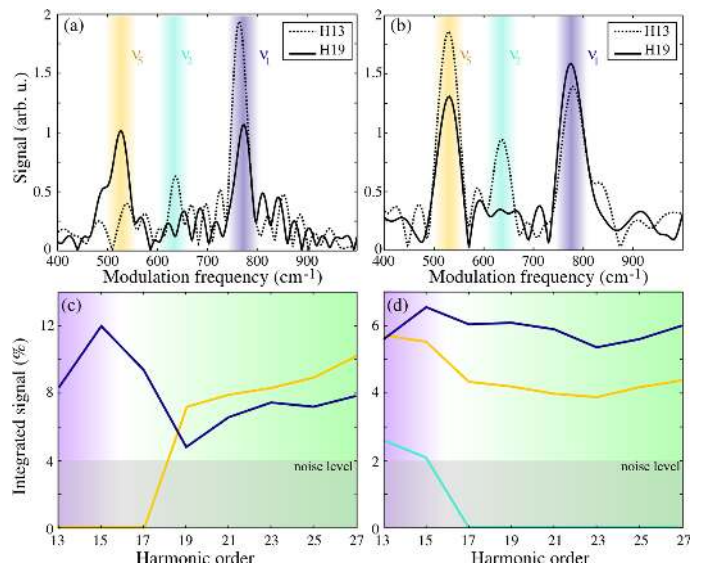

FIG. 7: The modulation of high harmonic generation by specific vibrations in ground state SF_6 molecules. Fourier transform of the intensity (a) and phase (b) modulations with pump-probe delay for harmonic 13 (dots) and 19 (line) showing the contribution of different Raman modes: υ_5-T_{2g} (524 cm^{-1}, yellow), υ_2-E_g (643 cm^{-1}, green) and υ_1-A_{1g} (774 cm^{-1}, blue). The contribution of each mode, obtained by integration of the peak in the FFT, is shown as a function of harmonic order in (c) intensity and (d) phase.

channel involved in the interferometer. First, changes in molecular geometry are expected to alter the vertical ionization potentials. Such modification influences the relative amplitude as well as the relative phase of each channel. For example, a 65 meV change in I_p results in a 100 mrad phase change for a plateau harmonic. Second, molecular vibrations can lift the electronic degeneracy of molecular orbitals, increasing the number of possible channels. Finally, any distortions of the molecular orbitals associated with these vibrations may affect both the ionization and recombination dipole moments.

We have performed pump-probe experiments using an intense ($\sim 7 \times 10^{13}$ W.cm^{-2}) 800 nm pulse to Raman-pump vibrational modes in the SF_6 molecules and produce high harmonics in the excited medium. In addition to conventional experiments in which the harmonic intensity is measured (Fig. 7(a,c)), we have used two-source interferometry to determine the evolution of the harmonic phase with pump-probe delay (Fig. 7(b,d)) [5, 33] (see Methods). The harmonic emission is periodically modulated as a function of pump-probe delay. The typical modulation depth of the harmonic signals are 5% for the intensity and 100 mrad for the harmonic phase. Three of the six normal modes of SF_6 are Raman active vibrations: υ_1-fully symmetric and strongly active mode A_{1g} with a quantum of 774 cm^{-1} (vibrational period of ≈ 43 fs), υ_2-the doubly degenerate mode E_g with a quantum of 643 cm^{-1} (≈ 52 fs) and finally the triply

degenerated v_5-T_{2g} mode with a quantum of 524 cm^{-1} ($\approx$ 63 fs) [34]. A Fourier analysis is performed to determine which vibrational modes modulate the signal (Fig. 7(a-b)).

The weight of each vibrational mode in the intensity and phase modulations is extracted by integrating the corresponding peak and normalizing to the total signal (Fig. 7(c-d)). The results show a clear transition around harmonic 17, consistent with the channel switching measured in static molecules. Below harmonic 17, in the region where the C channel dominates, the harmonic intensity is exclusively modulated by the v_1 mode. Above harmonic 17, the v_5 mode becomes slightly predominant. There is no significant contribution of the v_2 mode except for harmonic 13. Interestingly, the behavior of the harmonic phase is very different but also shows a transition associated to channel switching. The phase emission of C channel does not vary drastically for v_1 and v_5 nuclear dynamics and shows a weak contribution from v_2. The phase of the emission from the A channel seems insensitive to v_2 and dominated by v_1.

The complete calculation of the harmonic emission from vibrating molecules is beyond the scope of this article. As a first step, we evaluated the modifications of the strong field ionization yield resulting from molecular vibrations in the two dominant modes seen in the experiment: v_1 and v_5. For the C channel, ionization is maximized when the molecule is stretched in the v_1 mode, but shows no modulation in the v_5 mode. The ionization from the A channel shows modulations in both modes. This is in remarkable agreement with the measured modulations of the harmonic intensity (Fig. 7(c)), which suggests that when the strong field ionization yield is not modulated, neither is the recombination dipole moment.

II. DISCUSSION

Multi-channel high-harmonic generation in polyatomic molecules is a rich and complex process which initiates a broad range of multielectron phenomena. The identification and isolation of the different channels is a major challenge which requires the development and integration of new experimental tools. In this work we introduced and combined several experimental schemes in an advanced spectroscopic study, enabling us to resolve multi-channel SFI in SF$_6$. First, we identified the different SFI channels by performing wavelength-dependent CRATI measurements. Varying the wavelength addressed the issue of overlapping ATI combs which can occur at specific wavelengths, notably at the 800 nm driving frequency implemented in the majority of this work. We introduced a new scheme to HHG spectroscopy by resolving the spectral dependence of the normalized ellipticity response. This measure enabled isolation of the transverse shape of the electronic wavefunction at the moment of tunnel ionization, removing the complexity imposed by the additional steps of the interaction. We made use of the coherent properties of the process via RABBIT measurements which enabled the extraction of the relative phase between the channels. Such a measurement identified the important contribution of shape and autoionization resonances, hidden in many HHG measurements. Finally, we have made use of the nuclear degrees of freedom - via vibrational dynamics – as an important control knob which manipulates both the phase and amplitude associated with each channel, advancing our ability to identify the multi-channel nature of the interaction.

We believe that the methods presented here will illuminate the complexity and the rich spectroscopic information obscured in many HHG experiments. For example, coupled with accurate calculations of the multi-channel harmonic emission, our results should facilitate understanding the role of resonances in the emission process and also the elucidation of the influence of Jahn-Teller distortions in the ion [35].

The clear identification of the SFI channels is the first fundamental step in characterizing time-resolved multi-electron processes, the long term goal being to resolve charge migrations or field induced coupling between the channels. We believe that it will be possible to isolate such dynamics by increasing the dimensionality of the experiment – by scanning the fundamental wavelength of the strong laser field in HHG. Such scanning will scale the interferometer, presented in Fig. 1, enabling the decoupling of the different degrees of freedom involved in the process. Disentangling, for example, the contribution of resonances from dynamic features will be an important tool in HHG spectroscopy. In summary, we believe that the combination of methods presented here constitute an important building block for strong field spectroscopy and will lead to the discoveries of a broad range of multielectron strong field phenomena in complex targets such as polyatomic molecules.

III. METHODS

A. Channel-resolved Above-Threshold Ionization

Experiments were performed using a Legend Elite Duo laser system (Coherent Inc.) that delivered 35 fs, 3.1 mJ, 800 nm pulses at 1 kHz (Molecular Photonics laboratory, NRC Ottawa). Laser fundamental pulses were implemented directly in the 800 nm experiments whereas $\sim$40 fs 400 nm pulses were generated through second harmonic generation in thin β-BaBO$_4$ crystals (150 μm thick). $\sim$40 fs 480 nm, 532 nm and 590 nm pulses were generated through sum frequency generation of the signal pulses from an optical parametric amplifier (Light Conversion, TOPAS-C) and the fundamental beam in thin β-BaBO$_4$ crystals (250 μm thick). Laser pulses were focused with a f=50 cm spherical mirror onto a continuous, neat expansion of SF$_6$ molecules (expanded through a 50 μm pinhole $\sim$60 cm from the laser-molecular beam

interaction region in a differentially pumped chamber). The molecular beam PEPICO (Photo-Electron Photo-Ion COincidence) spectrometer used to collect the resulting photoelectrons and photoions has been described elsewhere [17]. Briefly, the kinetic energies of the photoelectrons were resolved by time-of-flight using a wide-bore permanent magnet, magnetic bottle spectrometer. Photoions were collected using a coaxial pulsed-field Wiley-McClaren time-of-flight mass spectrometer. The photoelectron and photoion time-of-flight signals were post-processed using a covariance analysis [36, 37] to correlate specific electron signals with the dominant SF_5^+ ions. The typical exponential ATI decay in energy has been substracted to enhance the ATI oscillations. This has to be described in the text (or methods).The resulting ATI spectra and experimental intensities were calibrated by argon and xenon ATI spectra recorded as a function of laser intensity.

B.   Calculations of strong field ionization rates

Bound-state neutral and cation wavefunctions were calculated using aug-cc-pVTZ basis set [38], large-core effective core potentials [39], and RASSCF wavefunctions with 35 (cation) or 36 (neutral) electrons in 25 orbitals, allowing single and double excitations. For the cation, the active space was optimized for an equally-weighted average of the six lowest states of the cation (X through D). The RASSCF vertical IPs were shifted uniformly by -0.512 eV. At the equilibrium O_h geometry (R(S-F)=1.575 Angstrom), the resulting cation state energies are within 0.3 eV of the correlated MCQDPT2(27/28,21)/aug-cc-pVTZ values.

The magnitude of the vibrational distortions induced by an impulsive Raman pump was determined [40] from normal vibrational modes and dipole polarizabilities, calculated at the CCSD/aug-cc-pVTZ level [41]. Calculated displacements assumed pump energy flux of ≈ 8.4 J cm^{-2}. Pump and probe polarizations were assumed to be collinear, and were integrated on an order-9 Lebedev grid [42]. RASSCF and MCQDPT2 [44] calculations were performed with GAMESS-US [43]. CCSD calculations used CFOUR [45]. Strong-field ionization calculations [20, 21] used Cartesian product grid with 0.18 Bohr spacing, extending to +/-18 Bohr from the origin, with an absorbing boundary [46] of 9.4 Bohr at the box edges. The simulation used 14 spatial channels, corresponding to the X, A, B, C, and D final states of the cation. Both laser and correlation coupling terms were included. Leap-frog time evolution used a time step of 0.003 atomic units.

C.   High-order harmonic spectroscopy

The high-harmonic spectroscopy experiments were performed using the Aurore laser system at CELIA, which delivers 28 fs, 7 mJ, 800 nm pulses at 1kHz. High harmonics were generated by focusing the pulses with a f=50 cm lens in a continuous jet produced by a 250 μm nozzle backed by a few hundred mbars of gas. The emitted radiation was analyzed by an extreme ultraviolet spectrometer (1200 mm^{-1} grating, dual Micro Channel Plates and a CCD camera).

To manipulate the laser ellipticity, two broadband zero-order waveplates were inserted in the laser beam: a motorized half waveplate in front of a fixed quarter waveplate. The harmonic signal was recorded as a function of the angle α between the half and quarter waveplate axis which determines the laser ellipticity $\epsilon = tan(2\alpha)$.

For RABBIT measurements, we used the experimental setup described in [47]. Briefly, the harmonic and infrared beams were delayed using a beam-splitting dichroic delay-line. They were focused by a toroidal mirror in a magnetic bottle time-of-flight spectrometer which recorded the electron spectrum produced by photoionizing argon atoms, as a function of delay between XUV and infrared beams.

Phase-resolved pump-probe experiments were performed by using a 0-π phase mask [33] inserted on the harmonic generating beam, before focusing. This mask created an interference pattern at focus, which resulted in the creation of two harmonic sources spatially separated by ~ 100 μm. In the far field these sources produced an interference patern, similar to Young's slits. A 800 nm pump beam was superimposed on one of the two sources, exciting the molecules by impulsive stimulated Raman scattering. The evolution of the phase of the harmonic emission as a function of pump probe delay was measured by determining the shift of the interference fringes, using a spatial Fourier transform.

IV.   ACKNOWLEDGEMENTS

[1] Keldysh, L. Ionization in the field of a strong electromagnetic wave. *Sov. Phys. JETP* **20**, 1307 (1965).

[2] Muth-Böhm, J., Becker, A. & Faisal, F. H. M. Suppressed molecular ionization for a class of diatomics in intense femtosecond laser fields. *Physical Review Letters* **85**, 2280–2283 (2000).

[3] Tong, X. M., Zhao, Z. X. & Lin, C. D. Theory of molecular tunneling ionization. *Physical Review A* **66**, 033402 (2002).

[4] Lezius, M. *et al.* Nonadiabatic Multielectron Dynamics in Strong Field Molecular Ionization *Phys. Rev. Lett.* **86**, 51–54. (2001).

[5] Smirnova, O., Patchkovskii, S., Mairesse, Y., Dudovich, N. & Ivanov, M. Y. Strong-field control and spectroscopy of attosecond electron-hole dynamics in molecules. *Proceedings of the National Academy of Sciences* **106**, 16556–16561 (2009).

[6] Haessler, S. *et al.* Attosecond imaging of molecular electronic wavepackets. *Nature Physics* **6**, 200–206 (2010).

[7] Agostini, P., Fabre, F., Mainfray, G., Petite, G. & Rahman, N. K. Free-free transitions following six-photon ionization of xenon atoms. *Phys. Rev. Lett.* **42**, 1127–1130 (1979).

[8] McPherson, A. *et al.* Studies of multiphoton production of vacuum-ultraviolet radiation in the rare gases. *J. Opt. Soc. Am. B* **4**, 595 (1987).

[9] Corkum, P. B. Plasma perspective on strong field multiphoton ionization. *Physical Review Letters* **71**, 1994–1997 (1993).

[10] Krause, J. L., Schafer, K. J. & Kulander, K. C. High-order harmonic generation from atoms and ions in the high intensity regime. *Physical Review Letters* **68**, 3535–3538 (1992).

[11] Lewenstein, M., Balcou, P., Ivanov, M. Y., L'Huillier, A. & Corkum, P. B. Theory of high-harmonic generation by low-frequency laser fields. *Physical Review A* **49**, 2117–2132 (1994).

[12] Le, A.-T., Lucchese, R., Tonzani, S., Morishita, T. & Lin, C. Quantitative rescattering theory for high-order harmonic generation from molecules. *Physical Review A* **80**, 013401 (2009).

[13] McFarland, B., Farrell, J., Bucksbaum, P. & Gühr, M. High-order harmonic phase in molecular nitrogen. *Physical Review A* **80**, 033412 (2009).

[14] Mairesse, Y. *et al.* High harmonic spectroscopy of multichannel dynamics in strong-field ionization. *Physical Review Letters* **104**, 213601 (2010).

[15] Shafir, D. *et al.* Resolving the time when an electron exits a tunneling barrier. *Nature* **485**, 343–346 (2012).

[16] Lee, K.F., Villeneuve, D.M., Corkum, P.B., Stolow, A. & Underwood, J.G. Field-Free Three-Dimensional Alignment of Polyatomic Molecules. *Physical Review Letters* **97**, 173001 (2006).

[17] Boguslavskiy, A. E. *et al.* The multielectron ionization dynamics underlying attosecond strong-field spectroscopies. *Science* **335**, 1336–1340 (2012).

[18] Paul, P. M. *et al.* Observation of a train of attosecond pulses from high harmonic generation. *Science* **292**, 1689 (2001).

[19] Haessler, S. *et al.* Phase distortions of attosecond pulses produced by resonance-enhanced high harmonic generation. *New Journal of Physics* **15**, 013051 (2013).

[20] Spanner, M. and Patchkovskii, S. One-electron ionization of multielectron systems in strong nonresonant laser fields. *Phys. Rev. A* **80**, 063411 (2009).

[21] Spanner, M. & Patchkovskii, S. Molecular strong field ionization and high harmonic generation: A selection of computational illustrations. *Chemical Physics* **414**, 10–19 (2013).

[22] Kanai, T., Takahashi, E. J., Nabekawa, Y. & Midorikawa, K. Destructive interference during high harmonic generation in mixed gases. *Phys. Rev. Lett.* **98**, 153904 (2007).

[23] Smirnova, O., Patchkovskii, S., Mairesse, Y., Dudovich, N. & Ivanov, M. Y. Strong-field control and spectroscopy of attosecond electron-hole dynamics in molecules. *Proceedings of the National Academy of Sciences* **106**, 16556–16561 (2009).

[24] Yang, L. *et al.* Energy-dependent valence photoelectron spectra of SF6. ab initio calculations and measurements. *Journal of Electron Spectroscopy and Related Phenomena* **94**, 163–179 (1998).

[25] Holland, D. M. P., Shaw, D. A., Hopkirk, A., MacDonald, M. A. & McSweeney, S. M. A study of the absolute photoabsorption cross section and the photoionization quantum efficiency of sulphur hexafluoride from the ionization threshold to 420 a. *Journal of Physics B: Atomic, Molecular and Optical Physics* **25**, 4823–4834 (1992).

[26] Stener, M., Toffoli, D., Fronzoni, G. & Decleva, P. Time dependent density functional study of the photoionization dynamics of SF6. *The Journal of Chemical Physics* **124**, 114306–114306–13 (2006).

[27] Lyngå, C., L'Huillier, A. & Wahlström, C.-G. High-order harmonic generation in molecular gases. *Journal of Physics B: Atomic, Molecular and Optical Physics* **29**, 3293–3302 (1996).

[28] Ivanov, M. Y., Brabec, T., & Burnett, N. Coulomb corrections and polarization effects in high-intensity high-harmonic emission. *Physical Review A* **54**, 742 (1996).

[29] Murray, R., Spanner, M., Patchkovskii, S. & Ivanov, M. Tunnel ionization of molecules and orbital imaging. *Physical Review Letters* **106**, 173001 (2011).

[30] Mairesse, Y. *et al.* Attosecond synchronization of high-harmonic soft x-rays. *Science* **302**, 1540 (2003).

[31] Rothhardt, J. *et al.* Amplitude and phase of resonant high harmonic emission in SF6. In *Laser Science*, OSA Technical Digest (online), LW1H.6 (Optical Society of America, 2012).

[32] Wagner, N. L. *et al.* Monitoring molecular dynamics using coherent electrons from high harmonic generation. *Proceedings of the National Academy of Sciences* **103**, 13279–13285 (2006).

[33] Camper, A. *et al.* High-harmonic phase spectroscopy using a binary diffractive optical element. *Phys. Rev. A* **89**, 043943 (2014).

[34] Boudon, V., Doménech, J. L., Bermejo, D. & Willner, H. High-resolution raman spectroscopy of the $\nu 1$ region and Raman–Raman double resonance spectroscopy of the $2\nu 1$-$\nu 1$ band of 32SF6 and 34SF6. determination of the equilibrium bond length of sulfur hexafluoride. *Journal of Molecular Spectroscopy* **228**, 392–400 (2004).

[35] Walters, Z. B., Tonzani, S. & Greene, C. H. Vibrational interference of raman and high harmonic gener-

ation pathways. *Chemical Physics* **366**, 103–114 (2009).

[36] Frasinski, L. *et al.* Molecular H_2 in intense laser fields probed by electron-electron, electron-ion, and ion-ion covariance techniques. *Phys. Rev. A* **46**, R6789 (1992).

[37] Mikosch, J. & Patchkovskii, S. Coincidence and covariance data acquisition in photoelectron and -ion spectroscopy. i. formal theory. *Journal of Modern Optics* **60**, 1426–1438 (2013).

[38] Woon, David E. and Dunning, Thom H. Gaussian basis sets for use in correlated molecular calculations. III. The atoms aluminum through argon. *The Journal of Chemical Physics* **98**, 1358 (1993).

[39] Bergner, A. *et al.* Ab initio energy-adjusted pseudopotentials for elements of groups 1317. *Molecular Physics* **6**, 1431 (1993).

[40] De Silvestri S. *et al.* Femtosecond time-resolved measurements of optic phonon dephasing by impulsive stimulated raman scattering in -perylene crystal from 20 to 300 K . *Chem. Phys. Lett.* **116**, 145 (1985).

[41] Kallay, M. and Gauss, J. Calculation of frequency-dependent polarizabilities using general coupled-cluster models . *Journal of Molecular Structure: {THEOCHEM}*

768, 71 (2006).

[42] V. I. Lebedev Values of the nodes and weights of ninth to seventeenth order gauss-markov quadrature formulae invariant under the octahedron group with inversion. *Zhvychmat* **15**, 48 (1975).

[43] Schmidt, M. W. *et al.* General Atomic and Molecular Electronic Structure System. *Journ. Comput. Chem.* **14**, 1347 (1993).

[44] Nakano, H. Quasidegenerate perturbation theory with multiconfigurational self-consistent-field reference functions. *Journ. of Chem. Phys.* **99**, 7983 (1993).

[45] Stanton, J. F., Gauss, J. *et al.* CFOUR, Coupled-Cluster techniques for Computational Chemistry, a quantum-chemical program package. *http://www.cfour.de.*

[46] Manolopoulos, D. E. Derivation and reflection properties of a transmission-free absorbing potential. *Journ. of Chem. Phys.* **117**, 9552 (2002).

[47] Loch, R. A. *et al.* Phase characterization of the reflection on an extreme UV multilayer: comparison between attosecond metrology and standing wave measurements. *Optics Letters* **36**, 3386–3388 (2011).